

Canonical Clocks and Hidden Geometric Freedom in Self-Imaging

Layton A. Hall* and Samuel Alperin†

Los Alamos National Laboratory, Los Alamos, New Mexico 87545, USA

Self-imaging represents a core hallmark of paraxial (quadratic)-wave evolution; yet, across its many realizations and generalizations over the past two centuries, the uniformity of recurrence planes along the propagation axis has been considered fundamental. However, by reframing the general phenomenon of self-imaging within its natural symplectic framework, we show that all self-imaging effects are necessarily tied to uniformly periodic recurrences in the canonical evolution coordinate – metaplectic time – and that the correspondence of that coordinate to the physical propagation axis represents an unexplored degree of freedom, which can be engineered arbitrarily by the initial transverse phase structure. Using a single programmable spatial light modulator, we demonstrate the construction of Talbot carpets characterized by recurrence spacings that accelerate and decelerate along the propagation axis, as well as those that follow polynomial, exponential, and sinusoidal axial trajectories, all of which preserve exact reconstruction in the canonical metaplectic time. These results establish metaplectic time as the fundamental invariant of self-imaging and reveal a regime of controllable axial dynamics previously thought to be fixed.

Self-imaging is one of the most striking and long-studied features of paraxial – quadratic – wave propagation – since Talbot’s original observation in 1836 [1] and derivation by Rayleigh in 1881 [2], it has been understood that under free-space propagation, any wave with transverse periodic structure, such as that of a plane-wave passed through a grating, undergoes exact reconstructions at periodic propagation distances. In the nearly two-centuries since the introduction of this seminal effect, the same quadratic wave evolution seen in paraxial optics has come to be recognized as the canonical form of wave propagation across classical and semi-classical settings, and as such, self-imaging has found applications ranging from structured-illumination microscopy [3] to temporal cloaking [4] and prime-number decomposition [5], and has been observed in nonlinear optics [6], quantum optics [7], and atomic matter waves [8, 9], demonstrating its universality across wave physics [10]. Numerous generalizations have expanded the scope of self-imaging to aperiodic structures [11, 12], rotating self-imaging planes [13], and accelerating transverse trajectories such as Airy-Talbot carpets [14–16].

However, despite the myriad extensions and generalizations of the original effect of self-imaging, a single feature has remained unchanged: up to deviations treated either as experimental imperfections or perturbative departures from the core effect, the recurrence planes have always occurred at *uniform* intervals along the physical propagation axis.

In this Letter, we show that the apparent rigidity of the uniform recurrence spacing is not fundamental to self-imaging phenomena, instead arising from the implicit assumption that the physical propagation coordinate z is the natural parameter of evolution for self-imaging. Specifically, we find that when quadratic wave evolution is instead expressed in its natural symplectic formulation – where propagation acts as a canonical transformation on the transverse phase space (x, k_x) [17–19] – a qualitatively different structure emerges. The associated metaplectic operator [20–23] advances the field in a unique

canonical coordinate $B = M_{12}$, which we term the *metaplectic time*. This canonical parameter advances uniformly under any quadratic Hamiltonian and is therefore the parameter in which self-imaging recurrences are intrinsically periodic. However, within this treatment it becomes clear that the laboratory axis z represents merely one possible embedding of this canonical clock, and the observed axial structure depends entirely on how the optical system maps B into z .

This distinction uncovers a latent degree of freedom in self-imaging – the transverse phase profile determines the curvature term in the symplectic generator and thereby sculpts the embedding $B(z)$. Uniform Talbot spacing occurs only when this embedding is affine; nonlinear embeddings cause the same uniform canonical recurrences to appear with accelerating, decelerating, or otherwise structured intervals in real space—while preserving exact self-imaging in metaplectic time. Thus, axial control of self-imaging, long assumed inaccessible, becomes possible by treating z not as the evolution parameter but as a coordinate subordinated to the canonical flow.

Using this theoretical framework, we experimentally demonstrate the ability to arbitrarily sculpt the embedding of the metaplectic time in physical space with a single programmable spatial light modulator. By imprinting controlled transverse phases on a periodic field, we realize accelerating and decelerating Talbot sequences as well as fully engineered recurrence patterns described by polynomial, exponential, and sinusoidal functions. The observed recurrence positions match the predicted values $z_k = B^{-1}(k\Delta B)$, confirming that metaplectic time is the natural invariant of self-imaging and revealing a regime of programmable axial Talbot dynamics that was previously inaccessible.

Theoretical Framework – The paraxial wave equation occupies a unique position in physics: it describes not only the evolution of optical beams in space but also the effective time evolution of quantum wave packets in two transverse dimensions. In both settings, the field obeys a Schrödinger-type equation, with the longitudinal coordinate—physical distance in optics, physical time in quantum mechanics—serving as the evolution parameter. Regardless of this physical interpretation, the underlying dynamics are generated by a quadratic

* laytonh@lanl.gov

† alperin@lanl.gov

Hamiltonian acting on the transverse phase space (x, k_x) . Propagation through any first-order (ABCD) system is therefore a canonical transformation represented by a real symplectic matrix $M = \begin{pmatrix} A & B \\ C & D \end{pmatrix} \in \text{Sp}(2, \mathbb{R})$, together with its associated metaplectic operator

$$U(x') = \frac{e^{ikDx'^2/2B}}{i\lambda|B|^{1/2}} \int U(x) e^{ik(Ax^2 - 2xx' + Dx'^2)/2B} dx. \quad (1)$$

Among the matrix elements, the off-diagonal term $B = M_{12}$ plays a distinguished role: it sets the scale of quadratic phase accumulation, normalizes the propagator, and determines the accumulated canonical phase in the metaplectic propagator. Because it governs the advance of the canonical flow, we refer to B as the *metaplectic time*. Unlike the laboratory evolution coordinate z , which depends on the geometry of a particular physical system, the metaplectic time is intrinsic to the wave dynamics and provides a unique, system-invariant clock.

To understand the implications of this structure for self-imaging, consider any field whose transverse angular spectrum contains a discrete set of wave vectors,

$$U_0(x) = \sum_j a_j e^{ik_{x,j}x}. \quad (2)$$

Under propagation through the metaplectic kernel (1), each angular component acquires a quadratic phase factor depending only on the canonical parameter B :

$$U_B(x') = e^{i\Theta(x', B)} \sum_j a_j \exp[-i\alpha B k_{x,j}^2] e^{ik_{x,j}x'}. \quad (3)$$

Self-imaging requires that all mode-dependent phases in Eq. (3) realign up to a single global phase. For a discrete spectrum $\{k_{x,j}\}$, this occurs exactly when

$$\alpha B (k_{x,j}^2 - k_{x,j'}^2) \in 2\pi\mathbb{Z} \quad \forall j, j'. \quad (4)$$

Whenever the squared wave numbers are commensurate, there exists a fundamental period ΔB such that all components realign when B advances by integer multiples of ΔB .

Thus the symplectic geometry of quadratic propagation leads to a striking and fully general conclusion: for *any* wavefield that admits exact self-imaging, its recurrences form a uniform sequence in the canonical coordinate B . Metaplectic time is the unique evolution parameter shared by all discrete-spectrum self-imaging phenomena—Talbot, fractional-Talbot, Montgomery, and their generalizations—and only at equally spaced values of B can all angular components realign.

Embedding canonical time into physical space – The formal detachment of the physically observed evolution coordinate from the canonical evolution immediately raises the question of how the two remain coupled. In other words: how does the physical propagation coordinate vary as a function of canonical time? In any optical system, the laboratory coordinate z is related to the canonical coordinate B by an embedding

$$B = B(z), \quad (5)$$

which depends entirely on the sequence of free-space sections and quadratic phase elements encountered by the field. Crucially, this dependence—including any nonlinearity—arises from the transverse phase profile $\phi(x)$ applied at the input plane.

A quadratic phase $\phi(x) = x^2/(2f)$ contributes a curvature $C = -1/f$ to the symplectic generator, while higher-order structure in $\phi(x)$ yields correspondingly higher-order dependence of $C(z)$ and therefore of $B(z)$ through the differential relation

$$\frac{d}{dz} \begin{pmatrix} A & B \\ C & D \end{pmatrix} = \begin{pmatrix} 0 & 1 \\ -C(z) & 0 \end{pmatrix} \begin{pmatrix} A & B \\ C & D \end{pmatrix}. \quad (6)$$

In geometric terms, the transverse phase $\phi(x)$ selects the vector field generating the canonical flow, and the physical coordinate is *pushed forward* along this flow to produce the embedding $B(z)$. The real-space recurrence planes can then be understood as the *pullback* of the uniform canonical lattice.

If ΔB denotes the fundamental metaplectic period (e.g. $\Delta B = d^2/\lambda$ for a grating), the axial positions z_k of the self-imaging planes satisfy the exact recurrence condition

$$B(z_k) = k \Delta B. \quad (7)$$

Equation (7) expresses the fact that the observed recurrence pattern is simply the inverse image of a uniformly spaced canonical sequence: $z_k = B^{-1}(k \Delta B)$.

To obtain the local axial spacing, we examine the difference between successive recurrence orders. From Eq. (7),

$$B(z_{k+1}) - B(z_k) = \Delta B.$$

By the mean value theorem, there exists a point $\xi_k \in (z_k, z_{k+1})$ such that $B'(\xi_k)(z_{k+1} - z_k) = \Delta B$, so that the exact spacing between adjacent recurrence planes is

$$\Delta z_k \equiv z_{k+1} - z_k = \frac{\Delta B}{B'(\xi_k)}, \quad (8)$$

with ξ_k lying between the two planes. When $B'(z)$ varies slowly over a single recurrence interval—which is the case for all embeddings realized here—one has $B'(\xi_k) \approx B'(z_k)$, and Eq. (8) reduces to the local spacing law

$$\Delta z_k \approx \frac{\Delta B}{B'(z_k)}. \quad (9)$$

In this form, Eq. (9) makes explicit that the apparent axial structure of any self-imaging sequence is governed entirely by the derivative of the embedding $B(z)$: affine embeddings produce uniformly spaced imaging planes, while nonlinear embeddings generate accelerating, decelerating, or otherwise structured recurrence patterns—even though the underlying evolution in the canonical coordinate remains perfectly uniform.

Accelerating Talbot Effects – For concreteness, we now specialize the general framework to the self-imaging of periodic gratings—the celebrated Talbot effect. A grating of period d produces an angular spectrum $k_{x,n} = 2\pi n/d$, corresponding to the projection of the two-dimensional phase-space Talbot

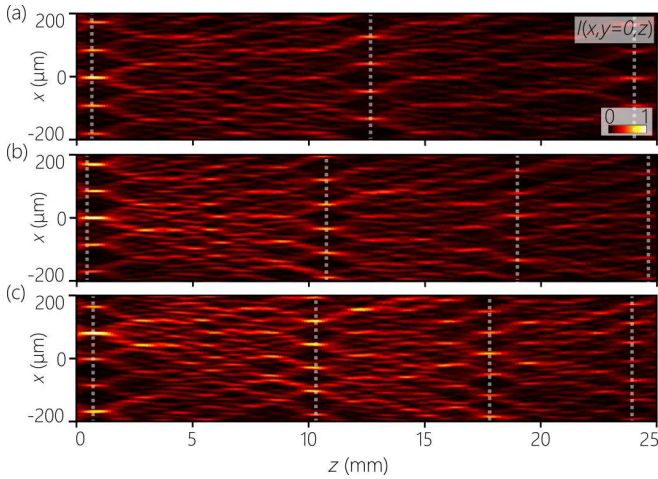


FIG. 1. Measurements of accelerating Talbot effect. Measured intensity $I(x, y = 0, z)$ with $d = 85 \mu\text{m}$ and $\lambda = 635 \text{ nm}$ for an effective focal length of (a) $f = \infty$, (b) 100 mm , and (c) 75 mm . White dotted lines mark the self-imaging planes for each case.

lattice onto the angular-frequency axis. Substituting these frequencies into Eq. (3) yields

$$U_B(x') = e^{i\Theta(x', B)} \sum_n c_n \exp \left[-i\pi n^2 \frac{\lambda B}{d^2} \right] e^{i2\pi n x'/d}, \quad (10)$$

so that the lattice realigns precisely when

$$B = \ell \frac{d^2}{\lambda}, \quad \ell \in \mathbb{Z}. \quad (11)$$

In this geometric picture, the Talbot distance d^2/λ is simply the basic unit of metaplectic time: the canonical period associated with the metaplectic phase. The axial Talbot pattern observed in real space is then determined not by changes in

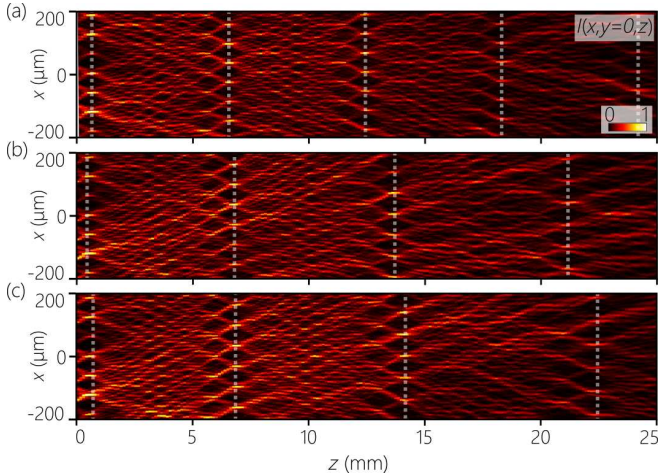


FIG. 2. Measurements of decelerating Talbot effect. Measured intensity $I(x, y = 0, z)$ with $d = 60 \mu\text{m}$ and $\lambda = 635 \text{ nm}$ for (a) $f = \infty$, (b) -100 mm , and (c) -75 mm . White dotted lines mark the self-imaging planes for each case.

the recurrence law but by the embedding $B(z)$ imposed by the optical system: affine embeddings yield uniform spacing, while nonlinear embeddings yield accelerating, decelerating, or arbitrarily structured sequences of Talbot planes.

Experimental Demonstration – While the theoretical framework developed above applies broadly to quadratic wave dynamics, classical optics provides a uniquely direct and highly controllable platform for probing its physical implications. In particular, a spatial light modulator (SLM) allows us to prepare a periodic field together with an arbitrary transverse phase profile $\phi(x)$, which fixes the curvature and higher-order structure of the beam at the launch plane. Because $\phi(x)$ determines the curvature term $C(z)$ and thereby the embedding $B(z)$, programming the SLM gives complete control over how the uniform canonical recurrence in metaplectic time is mapped into the laboratory coordinate. By translating a detector along z , we directly sample this embedding and reconstruct the axial recurrence pattern. See the Supplementary Material for experimental details.

We first benchmark the system using a reference grating of period $d = 85 \mu\text{m}$ with no imposed curvature. In this case, the embedding is affine, $B(z) = z$, and it predicts uniformly spaced Talbot planes with the standard period d^2/λ . The measured intensity $I(x, y = 0, z)$ indeed exhibits evenly spaced full- and half-Talbot planes at $\approx 23 \text{ mm}$ [Fig. 1(a)], confirming that the canonical evolution is faithfully represented in the laboratory coordinate for this baseline configuration.

To test the prediction that accelerating or decelerating Talbot sequences arise from nonlinear embeddings $B(z)$, we imprint a positive quadratic phase corresponding to focal length $f = 100 \text{ mm}$. This induces a forward canonical shear of the phase-space structure, reducing the derivative $B'(z)$ and therefore compressing the recurrence intervals according to $\Delta z_k \approx \Delta B/B'(z_k)$. The measured half-Talbot planes now occur at 11, 19, and 25 mm, in excellent agreement with the predicted mapping $B(z_k) = k\Delta B$. Increasing the curvature to $f = 75 \text{ mm}$ enhances this effect, yielding recurrence planes at 10, 18, and 24 mm [Fig. 1(c)].

Applying negative curvature produces the opposite behavior. For a grating with $d = 60 \mu\text{m}$, the unmodified configuration yields a Talbot distance of 11 mm. Introducing quadratic phases with $f = -100 \text{ mm}$ and $f = -75 \text{ mm}$ [Fig. 2], increasing $B'(z)$ and thereby expanding the recurrence intervals. The measured half-Talbot planes shift outward accordingly, confirming that the axial spacing is governed entirely by the derivative of the embedding $B(z)$ and not by any change to the canonical recurrence period.

Finally, by dynamically varying the phase applied to the constituent plane-wave components, we realize arbitrary embeddings $B(z)$, including polynomial, exponential, and sinusoidal forms. Representative measurements are shown in Fig. 3 for the case $d = 70 \mu\text{m}$. Quadratic, cubic, fractional-power, exponential, and sinusoidal embeddings each produce a characteristic axial pattern, and in every case the measured recurrence planes follow the predicted trajectories $z_k = B^{-1}(k\Delta B)$. Fig. 4 summarizes these results by plotting the measured half-Talbot positions for each embedding function, scaled by the linear Talbot distance. The agreement between experiment and theory

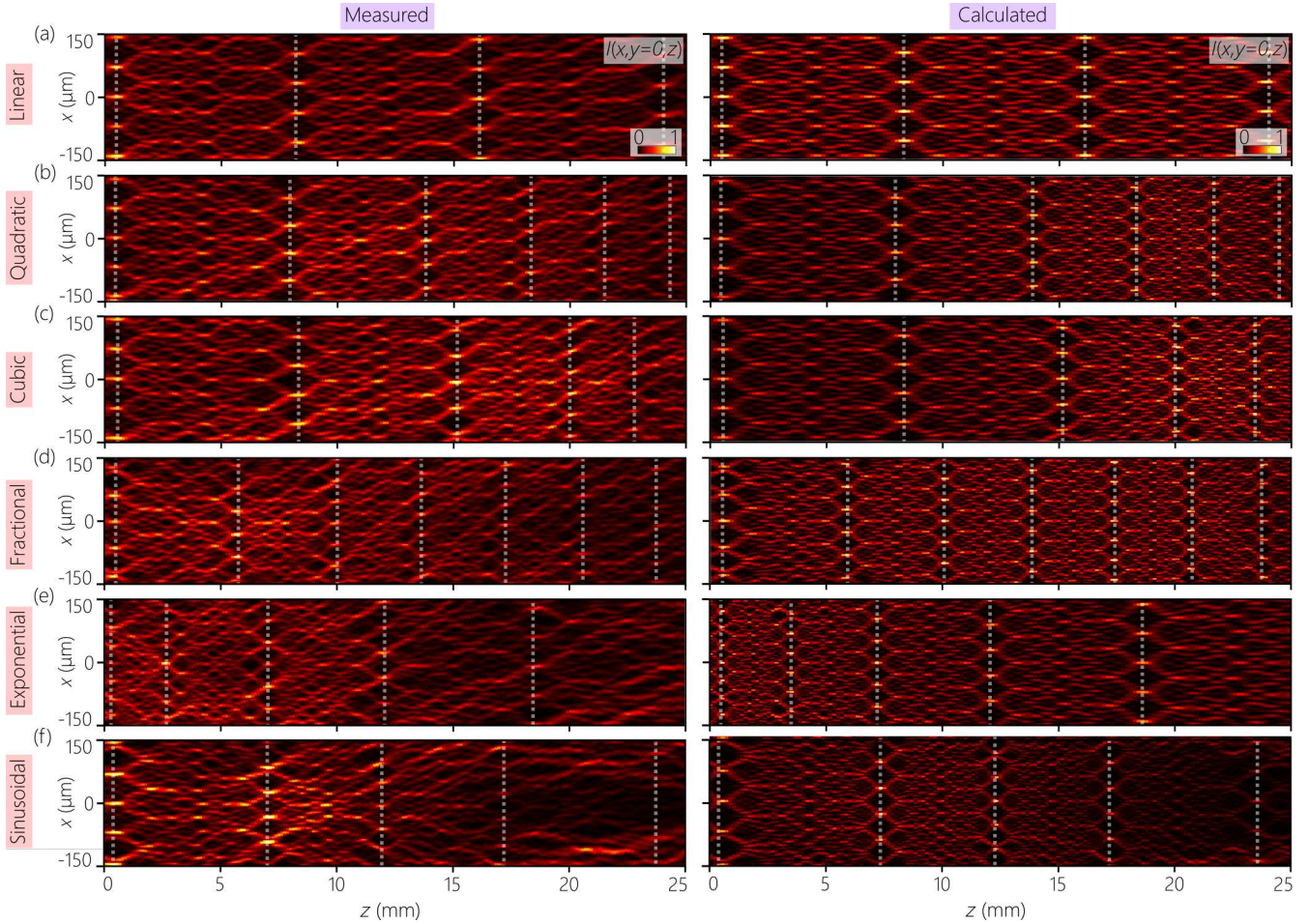


FIG. 3. Measurements and calculations of tailored Talbot effect. Intensity measurements of $I(x, y = 0, z)$ in the first column and calculated in the second column for varying conditions with initial period of $d = 70 \mu\text{m}$ for (a) linear Talbot effect, (b) quadratic acceleration with $z_k = z_T k + \delta z k^2$ condition with $\delta z/z_T = -0.08$, (c) cubic acceleration with $z_k = z_T k + \delta z k^3$ with $\delta z/z_T = -0.02$, (d) fractional acceleration with $z_k = z_T k + \delta z k^{5/4}$ with $\delta z/z_T = -0.325$, (e) exponential acceleration with $z_k = z_T k + \delta z e^{\alpha k}$ with $\delta z/z_T = 0.015$ and $\alpha = 1$ and (f) sinusoidal acceleration with $z_k = z_T k + \delta z \sin(2\pi k/\alpha)$ with $\delta z/z_T = 0.15$ and $\alpha = 1$ where k is the numbered self-imaging plane.

across all functional forms demonstrates that the axial structure of the Talbot effect can be arbitrarily sculpted through the programmed control of the transverse phase.

Taken together, these measurements directly visualize the central claim of the metaplectic framework: self-imaging is uniformly periodic only in the canonical coordinate B , and the apparent diversity of axial patterns arises solely from the geometry of the embedding $B(z)$. By programming $\phi(x)$, we program $B(z)$; by measuring along z , we observe the pullback of the canonical lattice. The experiment, therefore, establishes a practical route to arbitrary control of self-imaging phenomena and provides a quantitative demonstration of metaplectic time as the natural invariant parameter of quadratic wave evolution.

Discussion Our experimental results confirm a central prediction of the metaplectic formulation of quadratic wave evolution: all self-imaging phenomena, regardless of geometry, share a single invariant periodicity in the canonical coordinate B . The apparent diversity of Talbot, fractional-Talbot, Montgomery, and generalized self-imaging behaviors is therefore not the

result of different physical mechanisms but of different embed-

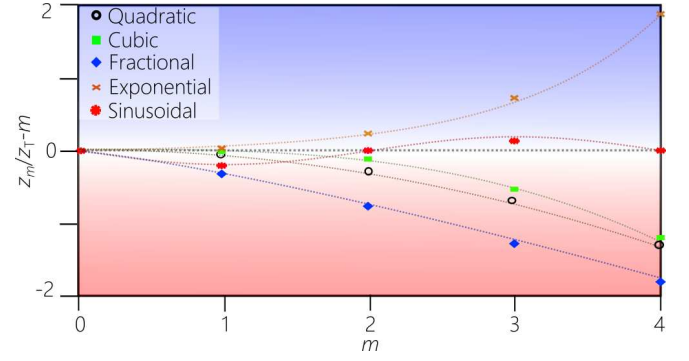


FIG. 4. Plot of arbitrary Talbot self-imaging planes. Plots of the measurements in Fig. 3 of the half self-imaging planes for the quadratic (black empty circle), cubic (green square), fractional (blue diamond), exponential (orange x), and sinusoidal (red full circle).

dings of this same invariant canonical time into the laboratory coordinate. By using a programmable SLM to sculpt $B(z)$, we directly visualize this embedding and demonstrate that the axial Talbot sequence may be freely accelerated, decelerated, or shaped according to arbitrary functional forms without disturbing the underlying metaplectic periodicity.

This perspective unifies several previously distinct lines of inquiry. Earlier studies reported modified Talbot distances for curved or spherical wavefronts, but these were treated as isolated geometrical corrections. Within the metaplectic framework, such effects are seen as special cases of nonlinear embeddings $B(z)$, and the experimental results here validate this interpretation by extending it to polynomial, exponential, and sinusoidal embeddings inaccessible to passive optical elements. In this sense, the SLM functions as a direct laboratory interface to the symplectic geometry of wave propagation: by programming the transverse phase, one programs the canonical flow itself.

The implications of this point of view extend beyond classical optics. Because the paraxial wave equation is mathematically equivalent to the two-dimensional Schrödinger equation, the same invariant periodicity in canonical time governs quantum revivals, matter-wave Talbot effects, and coherent atomic wave-packet evolution. The embedding $B(t)$ in those systems is fixed by the physical Hamiltonian, whereas here we can shape it arbitrarily, suggesting possible analog simulations of quantum revival engineering. Related ideas apply to acoustics, electron optics, and spatiotemporal analogues of the Talbot effect, where self-imaging occurs along time rather than space.

The metaplectic perspective also provides a natural framework for generalizations of self-imaging. The Montgomery effect, in which rotating self-images occur without axial periodicity in intensity, fits cleanly into this picture as a two-dimensional discrete spectrum on a phase-space conic. Extending the present methods to full two-dimensional phase-space control would enable arbitrary embeddings on such conics, opening the possibility of structured Montgomery revivals or hybrid Talbot–Montgomery dynamics. Likewise, the curvature and orientation of phase-space lattices suggest unexplored beam families whose evolution is dictated directly by their symplectic geometry.

Moreover, the metaplectic formulation also clarifies the well-known space–time duality [24] of quadratic wave dynamics, under the correspondence $x \leftrightarrow t$ and $k_x \leftrightarrow \omega$. As a result, paraxial diffraction maps directly onto dispersive temporal propagation under group-velocity dispersion, and spatial Talbot self-imaging yields a temporal analogue in the self-imaging of periodic pulse trains. Within this duality, the current results suggest that temporal Talbot recurrences are also consistently periodic solely when observed in the canonical evolution coordinate B , rather than in physical laboratory time. Nonlinear embeddings of metaplectic time into the temporal coordinate—implemented, for example, through engineered dispersion [25] or time-lens systems [26]—would therefore produce accelerating, decelerating, or otherwise structured temporal self-imaging while preserving exact canonical periodicity. This suggests that metaplectic time provides a unifying invariant for both spatial and temporal self-imaging phenomena across quadratic wave systems, and points toward generalizations in which tailored phase-space control enables effective non-quadratic Hamiltonian engineering beyond the strictly quadratic class [27].

Finally, the ability to control $B(z)$ with high precision suggests connections to number theory and spectral engineering. Because the canonical recurrence condition $B = \ell \Delta B$ mirrors the structure of quadratic Gauss sums, programmable embeddings may offer a route to optical implementations of arithmetic transforms. The demonstration of arbitrary recurrence paths (Fig. 3) points toward such possibilities by showing that metaplectic time can be discretized, warped, or modulated while maintaining coherent reconstruction.

Overall, the results establish metaplectic time as a powerful and conceptually unifying parameter for wave dynamics across physics. The ability to sculpt its embedding into real space provides an entirely new degree of control over self-imaging phenomena, transforming a classical diffraction effect into a versatile platform for exploring canonical geometry, wave recurrence, and programmable Hamiltonian evolution.

Acknowledgments L.A.H. acknowledges Los Alamos National Laboratory LDRD program grant 20251140PRD1. S. A. acknowledges Los Alamos National Laboratory LDRD program grant 0230865PRD3. We thank Michael Martin for the use of the equipment and space for these experiments.

[1] H. F. Talbot, Facts relating to optical science. No. IV, *Philos. Mag.* **9**, 401 (1836).

[2] L. Rayleigh, XXV. On copying diffraction-gratings, and on some phenomena connected therewith, *Philos. Mag.* **11**, 196 (1881).

[3] S. Chowdhury, J. Chen, and J. A. Izatt, Structured illumination fluorescence microscopy using Talbot self-imaging effect for high-throughput visualization, *arXiv:1801.03540* (2018).

[4] B. Li, X. Wang, J. Kang, Y. Wei, T. Yung, and K. K. Y. Wong, Extended temporal cloak based on the inverse temporal Talbot effect, *Opt. Lett.* **42**, 767 (2017).

[5] K. Pelka, J. Graf, T. Mehringer, and J. von Zanthier, Prime number decomposition using the Talbot effect, *Opt. Express* **26**, 15009 (2018).

[6] Y. Zhang, J. Wen, S. Zhu, and M. Xiao, Nonlinear Talbot effect, *Physical Review Letters* **104**, 183901 (2010).

[7] X.-B. Song, H.-B. Wang, J. Xiong, K. Wang, X. Zhang, K.-H. Luo, and L.-A. Wu, Experimental observation of quantum Talbot effects, *Physical Review Letters* **107**, 033902 (2011).

[8] M. S. Chapman, C. R. Ekstrom, T. D. Hammond, J. Schmiedmayer, B. E. Tannian, S. Wehinger, and D. E. Pritchard, Near-field imaging of atom diffraction gratings: The atomic Talbot effect, *Physical Review A* **51**, R14 (1995).

[9] C. Ryu, M. Andersen, A. Vaziri, M. d’Arcy, J. Grossman, K. Helmerson, and W. Phillips, High-order quantum resonances observed in a periodically kicked bose-einstein condensate, *Phys. Rev. Lett.* **96**, 160403 (2006).

[10] M. Berry, I. Marzoli, and W. Schleich, Quantum carpets, carpets of light, *Physics World* **14**, 39 (2001).

- [11] W. D. Montgomery, Self-imaging objects of infinite aperture, *J. Opt. Soc. Am.* **57**, 772 (1967).
- [12] M. Yessenov, L. Sacchi, A. Palmieri, L. A. Hall, A. F. Abouraddy, and F. Capasso, Observation of spatially structured montgomery effect in free space, arXiv:2510.16269.
- [13] R. Piestun and J. Shamir, Generalized propagation-invariant wave fields, *J. Opt. Soc. Am. A* **15**, 3039 (1998).
- [14] G. A. Siviloglou, J. Broky, A. Dogariu, and D. N. Christodoulides, Observation of accelerating Airy beams, *Phys. Rev. Lett.* **99**, 213901 (2007).
- [15] Y. Zhang, M. R. B. Hua Zhong, C. Li, Z. Zhang, F. Wen, Y. Zhang, and M. Xiao, Fractional nonparaxial accelerating Talbot effect, *Opt. Lett.* **41**, 3273 (2016).
- [16] Y. Lumer, L. Drori, Y. Hazan, and M. Segev, Accelerating self-imaging: the Airy-Talbot effect, *Phys. Rev. Lett.* **115**, 013901 (2015).
- [17] V. I. Arnold, *Mathematical Methods of Classical Mechanics*, 2nd ed. (Springer, New York, 1989).
- [18] V. Guillemin and S. Sternberg, *Symplectic Techniques in Physics* (Cambridge University Press, Cambridge, 1984).
- [19] J. E. Marsden and T. S. Ratiu, *Introduction to Mechanics and Symmetry*, Texts in Applied Mathematics, Vol. 17 (Springer, New York, 1999).
- [20] M. A. de Gosson, *Symplectic Methods in Harmonic Analysis and in Mathematical Physics* (Birkhäuser, Basel, 2011).
- [21] W. Miller, *Symmetry and Separation of Variables* (Addison-Wesley, Reading, MA, 1977).
- [22] J. W. Goodman, *Introduction to Fourier Optics*, 3rd ed. (Roberts and Company, Greenwood Village, CO, 2005).
- [23] A. W. Lohmann, Image rotation, wigner distribution, and the fractional fourier transform, *J. Opt. Soc. Am. A* **10**, 2181 (1993).
- [24] B. H. Kolner, Space-time duality and the theory of temporal imaging, *IEEE J. Quantum Electron.* **30**, 1951 (1994).
- [25] L. A. Hall, S. A. Ponomarenko, and A. F. Abouraddy, Temporal talbot effect in free space, *Opt. Lett.* **46**, 3107 (2021).
- [26] B. H. Kolner and M. Nazarathy, Temporal imaging with a time lens, *Opt. Lett.* **14**, 630 (1989).
- [27] M. Yessenov, L. A. Hall, and A. F. Abouraddy, Engineering the optical vacuum: Arbitrary magnitude, sign, and order of dispersion in free space using space-time wave packets, *ACS Phot.* **8**, 2274 (2021).

Canonical Clocks and Hidden Geometric Freedom in Self-Imaging: Supplemental Material

Layton A. Hall* and Samuel Alperin†
Los Alamos National Laboratory, Los Alamos, NM 87545, USA

Supplemental material including derivations and detailed description of experimental setup.

I. WDF OF A FIELD AT A PERIODIC GRATING

For completeness we derive the Wigner distribution function (WDF) of a coherent field at a one-dimensional periodic grating at the input plane $z = 0$. We use the (unnormalized) Wigner definition

$$W(x, k_x) = \int \psi^*(x + x'/2) \psi(x - x'/2) e^{ik_x x'} dx', \quad (1)$$

where $\psi(x)$ is the transverse field.

A. General periodic field

Consider a field that is strictly periodic with period d , so that it admits a Fourier series representation

$$\psi(x) = \sum_{n=-\infty}^{\infty} c_n e^{ink_d x}, \quad k_d = \frac{2\pi}{d}. \quad (2)$$

Substituting Eq. (2) into Eq. (1) gives

$$\begin{aligned} W(x, k_x) &= \int \left[\sum_m c_m^* e^{-imk_d(x+x'/2)} \right] \left[\sum_n c_n e^{ink_d(x-x'/2)} \right] e^{ik_x x'} dx' \\ &= \sum_{m,n} c_m^* c_n \int e^{-imk_d(x+x'/2)} e^{ink_d(x-x'/2)} e^{ik_x x'} dx'. \end{aligned} \quad (3)$$

Separating the x - and x' -dependence,

$$e^{-imk_d x} e^{ink_d x} = e^{i(n-m)k_d x}, \quad (4)$$

and

$$e^{-imk_d x'/2} e^{-ink_d x'/2} e^{ik_x x'} = \exp \left[i \left(k_x - \frac{m+n}{2} k_d \right) x' \right]. \quad (5)$$

We therefore obtain

$$W(x, k_x) = \sum_{m,n} c_m^* c_n e^{i(n-m)k_d x} \int e^{i(k_x - \frac{m+n}{2} k_d) x'} dx'. \quad (6)$$

The x' -integral is a delta distribution, so up to an overall normalization constant,

$$W(x, k_x) \propto \sum_{m,n} c_m^* c_n e^{i(n-m)k_d x} \delta \left(k_x - \frac{m+n}{2} k_d \right). \quad (7)$$

Eq. (7) shows that the Wigner support in k_x lies on discrete lines at $k_x = \frac{m+n}{2} k_d$, while along each such line the dependence on x is a Fourier series with spatial frequencies $(n-m)k_d$. This is the general phase-space structure of a coherently illuminated periodic grating at $z = 0$.

B. Dirac-comb grating and the phase-space lattice

The ideal Talbot object can be modeled as a Dirac-comb field

$$\psi(x) = \sum_{p=-\infty}^{\infty} \delta(x - pd), \quad (8)$$

representing an infinite array of narrow pinholes with period d . This field has a discrete Fourier series with equal-magnitude coefficients (up to normalization), so we may take $c_n = 1$ in Eq. (2) for the purpose of identifying the phase-space structure. Substituting $c_m = c_n = 1$ into Eq. (7) yields

$$W(x, k_x) \propto \sum_{m,n} e^{i(n-m)k_d x} \delta \left(k_x - \frac{m+n}{2} k_d \right). \quad (9)$$

It is convenient to introduce new indices

$$p = m + n, \quad q = n - m, \quad (10)$$

so that

$$m = \frac{p - q}{2}, \quad n = \frac{p + q}{2}. \quad (11)$$

The requirement $m, n \in \mathbb{Z}$ implies that p and q have the same parity. In terms of (p, q) , Eq. (9) becomes

$$W(x, k_x) \propto \sum_{\substack{p,q \in \mathbb{Z} \\ p \equiv q \pmod{2}}} e^{iqk_d x} \delta \left(k_x - \frac{p}{2} k_d \right). \quad (12)$$

Using the Poisson summation formula in q , this structure can be rewritten as a two-dimensional Dirac lattice in phase space,

$$W(x, k_x) \propto \sum_{m,\ell} w_{m,\ell} \delta \left(x - \frac{md}{2} \right) \delta \left(k_x - \ell \frac{2\pi}{d} \right), \quad (13)$$

where $w_{m,\ell} = \pm 1$ is a parity-dependent weight whose detailed form depends on the chosen normalization of $\psi(x)$.

C. Free-space propagation as a symplectic shear

Under paraxial free-space propagation, the field $\psi(x, z)$ obeys

$$i \frac{\partial}{\partial z} \psi(x, z) = -\frac{1}{2k_0} \frac{\partial^2}{\partial x^2} \psi(x, z), \quad (14)$$

where k_0 is the wavenumber. It is a standard result of phase-space optics that the corresponding Wigner function evolves under free-space propagation as a shear,

$$W(x, k_x; z) = W_0 \left(x - \frac{z}{k_0} k_x, k_x \right), \quad (15)$$

* laytonh@lanl.gov

† Alperin@lanl.gov

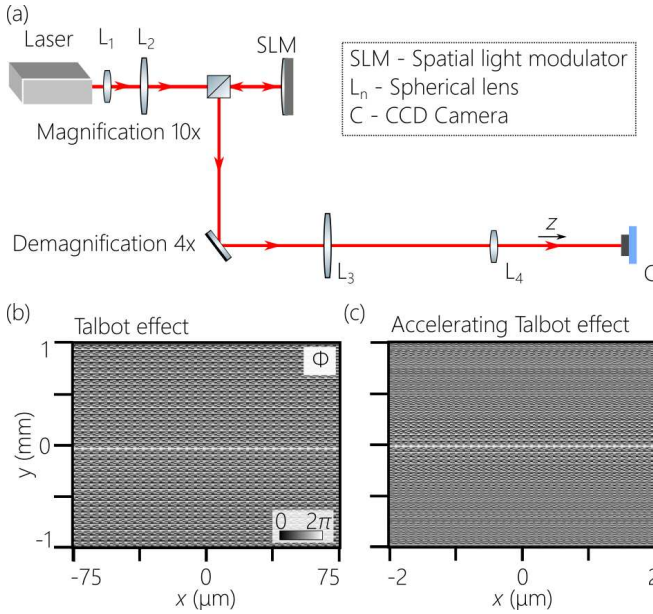


FIG. 1. **Accelerating Talbot synthesis.** (a) Experimental setup using a monochromatic source at $\lambda = 635$ nm. (b) Interleaved phase pattern on the SLM. (c) Interleaved phase pattern overlaid with quadratic curvature for accelerating Talbot dynamics.

where $W_0(x, k_x) \equiv W(x, k_x; 0)$ is the Wigner distribution at the input plane. Equation (15) expresses the fact that free space is generated by a quadratic Hamiltonian $H = k_x^2/2k_0$, so the phase-space trajectories are straight lines: points move along x -directions with velocity k_x/k_0 while k_x remains constant.

Applied to the Talbot lattice (13), this means that each lattice point (x_m, k_ℓ) evolves as

$$(x_m, k_\ell) \mapsto \left(x_m - \frac{z}{k_0} k_\ell, k_\ell \right), \quad (16)$$

so that the entire lattice is sheared horizontally as z increases. The Talbot and fractional-Talbot recurrences may be understood as propagation distances z for which this sheared lattice becomes congruent to itself modulo the underlying spatial and angular periodicity.

II. SYNTHESIS SETUP AND PHASE PATTERNS

The experimental setup is shown in Fig. 1(a). A continuous-wave laser at $\lambda = 635$ nm (Thorlabs HLS635) is expanded to a diameter of 10 mm and directed at normal incidence onto a spatial light modulator (SLM; Meadowlark HSP1K-488-800-PC8). The modulated beam is retro-reflected, passed through a 50:50 beam splitter, and relayed through a 4f imaging system composed of lenses with focal lengths $f_1 = 400$ mm and $f_2 = 100$ mm, resulting in a 4× demagnification. The output field is recorded using a CCD camera (Allied Vision 1800-U-500c) during axial scanning.

III. EXPERIMENTAL SYNTHESIS OF AXIALLY REPARAMETERIZED TALBOT FIELDS

We now describe the physical implementation by which a prescribed nonlinear axial mapping of the Talbot self-imaging planes is synthesized using a single phase-only spatial light modulator (SLM). The essential physical mechanism is the controlled redistribution of transverse wavevectors k_x across the grating spectrum by imposing a programmed transverse phase gradient. This modifies the longitudinal phase accumulation of each grating order and thereby reparameterizes the uniform metaplectic evolution into a nonlinear laboratory-coordinate recurrence.

A. Talbot geometry and spectral construction

An effective transverse lattice period L is defined in the SLM plane, which sets the fundamental Talbot distance

$$z_T = \frac{2L^2}{\lambda}, \quad (17)$$

where λ is the optical wavelength. The Talbot field is synthesized from a discrete set of M dominant grating orders with transverse wavevectors

$$k_{x,m} = \frac{2\pi m}{L}, \quad (18)$$

Each order is treated as an independent plane-wave component whose longitudinal phase evolution determines the axial self-imaging structure.

B. Programming the axial recurrence law

Axial reparameterization is introduced by prescribing a modulation function $f(z/z_T)$ that specifies the desired Talbot trajectory from the metaplectic time condition. Instead of invoking a physical refractive index, this modulation is implemented directly through controlled longitudinal phase accumulation corresponding to the metaplectic condition. We define a dimensionless deformation envelope

$$\eta(z) = 1 + \Delta\eta f\left(\frac{z}{z_T}\right), \quad (19)$$

where $\Delta\eta \ll 1$ sets the deformation strength. The corresponding longitudinal and transverse wavevector components are assigned as

$$k_{x,m}(z) = k_{x,m} \sqrt{\eta(z)}, \quad (20)$$

$$k_{z,m}(z) = k_0 - \frac{k_{x,m}^2}{2k_0} \eta(z), \quad (21)$$

with $k_0 = 2\pi/\lambda$. These relations specify the programmed dispersion experienced by each spectral order during propagation, without invoking a physical medium.

The local propagation angle of each order follows from

$$\theta_m(z) = \arctan\left(\frac{k_{x,m}(z)}{k_{z,m}(z)}\right), \quad (22)$$

which determines its transverse trajectory $x_m(z) = z \tan \theta_m(z)$. The transverse phase accumulated by each spectral component is then

$$\phi_m(z) = \int_0^z k_{x,m}(z') \frac{dx_m}{dz'} dz'. \quad (23)$$

This phase directly encodes the desired longitudinal change of each order.

C. Mapping longitudinal phase onto the SLM

To implement the programmed phases on the SLM, the trajectories $\phi_m(z)$ are inverted onto a uniform transverse SLM coordinate y using the parametric correspondence $y \leftrightarrow x_m(z)$. This yields a set of transverse phase profiles $\phi_m(y)$, one for each grating order. Each phase profile represents the spatial phase gradient required to generate the desired $k_{x,m}(z)$ evolution upon propagation.

The phase-only field for each order is therefore written as

$$\Psi_m(y) = \exp[i\phi_m(y)]. \quad (24)$$

D. Spatial multiplexing of grating orders

All four phase-modulated orders are encoded into a single SLM mask using deterministic spatial multiplexing. Binary selector functions $\chi_m(y)$ assign every N th SLM column to the corresponding order:

$$\Psi(y) = \sum_{m=1}^N \Psi_m(y) \chi_m(y). \quad (25)$$

This interleaving ensures that each spectral component experiences its independently programmed phase gradient while remaining mutually coherent upon propagation.

E. Phase-only encoding

Because the SLM supports phase-only modulation, the complex multiplexed field is converted into a realizable phase

pattern by extracting its argument,

$$\Phi_{\text{SLM}}(y) = \arg[\Psi(y)]. \quad (26)$$

This final phase mask simultaneously controls the longitudinal phase accumulation of all Talbot orders, thereby enforcing the prescribed axial recurrence law $f(z/z_T)$. By selecting different functional forms of f , we experimentally realize accelerating, decelerating, polynomial, fractional, exponential, and oscillatory Talbot sequences.

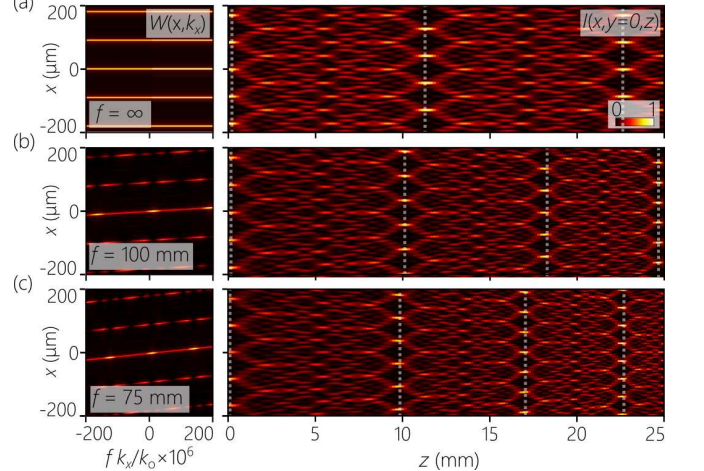


FIG. 2. Calculation of accelerating Talbot effect. Calculation of the phase space Wigner function $W(x, k_x)$ and measured intensity $I(x, y = 0, z)$ with $d = 85 \mu\text{m}$ and $\lambda = 635 \text{ nm}$ for an effective focal length of (a) $f = \infty$, (b) 100 mm, and (c) 75 mm. White dotted lines mark the self-imaging planes for each case.

Importantly, this procedure does not approximate or distort the self-imaging process. It preserves the exact discrete spectral correlations required for Talbot reconstruction while embedding the invariant metaplectic evolution into a nonlinear laboratory coordinate. The observed axial acceleration therefore arises purely from Hamiltonian phase-space control rather than from transverse beam bending or geometric tilt.

IV. CALCULATED RESULTS

We present the calculated results of the experiments seen in the main text. We use a Fourier transform method to calculate the intensity patterns from the initial phase pattern used in the experiments.

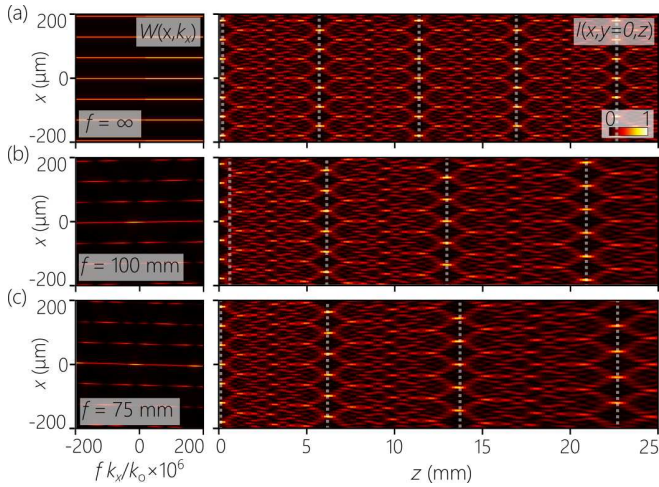


FIG. 3. Calculation of decelerating Talbot effect. Calculation of the phase space Wigner distribution function $W(x, k_x)$ and measured intensity $I(x, y=0, z)$ with $d = 60 \mu\text{m}$ and $\lambda = 635 \text{ nm}$ for (a) $f = \infty$, (b) -100 mm , and (c) -75 mm . White dotted lines mark the self-imaging planes for each case.